Error Rate Reduction of Single-Qubit Gates via Noise-Aware Decomposition

Thomas J. Maldonado,[1] Johannes Flick,[2] Stefan Krastanov,[3, 4] and Alexey Galda[5, 6, *]

[1]*Department of Physics, Harvard University, Cambridge, MA 02138, USA*
[2]*Center for Computational Quantum Physics, Flatiron Institute, 162 Fifth Avenue, New York, NY 10010, USA*
[3]*John A. Paulson School of Engineering and Applied Sciences, Harvard University, Cambridge, MA 02138, USA*
[4]*Department of Electrical Engineering and Computer Science,*
Massachusetts Institute of Technology, Cambridge, MA 02139, USA
[5]*James Franck Institute, University of Chicago, Chicago, IL 60637, USA*
[6]*Computational Science Division, Argonne National Laboratory, Lemont, IL 60439, USA*

(Dated: April 16, 2021)

In the current era of Noisy Intermediate-Scale Quantum (NISQ) technology, the practical use of quantum computers remains inhibited by our inability to aptly decouple qubits from their environment to mitigate computational errors. In this work, we introduce an approach by which knowledge of a qubit's initial quantum state and the standard parameters describing its decoherence can be leveraged to mitigate the noise present during the execution of a single-qubit gate. We benchmark our protocol using cloud-based access to IBM quantum processors. On `ibmq_rome`, we demonstrate a reduction of the single-qubit error rate by 38%, from 1.6×10^{-3} to 1.0×10^{-3}, provided the initial state of the input qubit is known. On `ibmq_bogota`, we prove that our protocol will never decrease gate fidelity, provided the system's T_1 and T_2 times have not drifted above 100 times their assumed values. The protocol can be used to reduce quantum state preparation errors, as well as to improve the fidelity of quantum circuits for which some knowledge of the qubits' intermediate states can be inferred. This work presents a pathway to using information about noise levels and quantum state distributions to significantly reduce error rates associated with quantum gates via optimized decomposition into native gates.

I. INTRODUCTION

Four decades after its conception [1], the quantum computer's (QC) far-reaching computational potential remains abundantly clear [2]. Among the various physical systems whose quantum properties can be harnessed for computation [3–6], superconducting transmon qubits have demonstrated promise in their ability to realize scalable QCs [7–9] and have accordingly been made available to the public via cloud-based services offered by private companies such as IBM, Rigetti Computing, Amazon, Microsoft, and Honeywell. Despite their recent increase in availability, in the era of Noisy Intermediate-Scale Quantum (NISQ) technology [10], our ability to utilize these machines to their full potential remains significantly inhibited by the computational errors that arise from interactions between the physical qubits and their environment.

While these detrimental interactions can be suppressed through the development of noise-resilient quantum hardware, the effective noise present during circuit execution can also be mitigated by optimizations in the compilation process [11]. Examples of software-based optimization protocols have been demonstrated across the full quantum computing stack, from high-level circuit depth compression via quantum-assisted quantum compiling [12] down to the optimization of individual native gates through the use of pulse-level control [13–15]. Some notable examples include noise tailoring via randomized compiling [16], dynamical decoupling of idle qubits [17], optimized state preparation via active reset [18, 19], and measurement via excited state promoted readout [20, 21].

In this work, we present a software-based optimization protocol used to reduce the error rate of a single-qubit gate by means of a noise-aware decomposition into native gates. The optimization of native gates themselves is a complementary task and a powerful noise-mitigation tool in its own right, but it requires pulse-level control, a level of hardware access both unfamiliar and inaccessible to many users of NISQ devices. The goal of this work is to demonstrate a reduction of single-qubit error rates without the need for this lower level of access. By optimizing the decomposition of single-qubit gates without improving the native gates themselves, we demonstrate the efficacy of a protocol that is straightforward to implement at the gate level and requires minimal knowledge of the underlying Hamiltonians governing the qubit dynamics during gate execution. Accordingly, it can be easily adapted for use in QCs based on arbitrary physical systems. In the sections to follow, we describe how to improve gate fidelity by leveraging knowledge of the input qubit's initial state, along with its characteristic coherence times T_1 and T_2. While we demonstrate our approach on two five-qubit IBM transmon devices, our optimization protocol is hardware-agnostic and assumes the two most prominent channels of Markovian noise in NISQ devices: relaxation and dephasing.

The structure of this paper is as follows. In Section II, we describe IBM's native gate set and how the compiler decomposes single-qubit gates into native gates. Section III builds on Section II by using the decomposition de-

fined therein to model the execution of a single-qubit gate in the presence of Markovian noise. Section IV concludes the definition of the protocol by outlining how the noise model defined in Section III can be used to optimize an arbitrary single-qubit gate acting on a known initial state. Section V details a randomized benchmarking (RB) [22] experiment on `ibmq_rome` [23] used to empirically determine the reduction of the single-qubit error rate offered by our optimizer when the initial state of the input qubit is known. Section VI outlines a RB experiment on `ibmq_bogota` [24] used to analyze the optimizer's sensitivity to coherence time drifts.

II. NATIVE GATES

We start by introducing IBM's native gate set and describing how the compiler of quantum circuits decomposes single-qubit gates[1] into native gates. An arbitrary rotation U on the Bloch sphere can be parameterized by its Euler angles [25]. Concretely, $\forall U \in SU(2)$, $\exists \alpha$, β, $\delta \in [0, 2\pi)$, $\gamma \in [0, \pi]$ such that

$$U(\beta, \gamma, \delta) = e^{i\alpha} R_z(\beta) R_y(\gamma) R_z(\delta) \tag{1}$$

where R_z and R_y are rotations about the z- and y-axes, respectively. Since a global phase enacted on a quantum state has no physical effect, the value of α is irrelevant. Effectively, Eq. (1) defines the decomposition of an arbitrary single-qubit gate into three rotations, two about the z-axis and one about the y-axis. In this paper, we work exclusively with the native gates used by IBM in their standard decomposition framework [26]: rotations about the x-axis by integer multiples of $\pi/2$ and rotations about the z-axis by an arbitrary angle. We note that, in principle, IBM's native gate set can be expanded using pulse-level control [13, 14], but in hopes of making our protocol easier to implement for those without this lower level of access, we maintain the standard native gate set described above. The decomposition outlined in Eq. (1) can be rewritten in terms of these native gates R_z and $R_x(\pm\pi/2)$:

$$U(\beta, \gamma, \delta) = e^{i\alpha} R_z(\beta) R_x(-\pi/2) R_z(\gamma) R_x(\pi/2) R_z(\delta) \tag{2}$$

Thus, any single-qubit gate can be applied via the sequential application of IBM's native gates defined by Eq. (2).

Before proceeding to the noise model, we make a brief note on the physical implementation of the basis gate set on IBM quantum processors [26]. IBM Quantum systems are built using fixed-frequency superconducting transmon qubits, wherein the qubits are manipulated using microwave pulses. The $R_x(\pm\pi/2)$ gates in the decomposition (2) are implemented using calibrated microwave pulses, while the R_z rotations are realized as

zero-duration "virtual" gates by adding a phase offset in software [27]. For the purposes of the noise model that we outline in the following section, it is important that microwave pulses of fixed shape and duration are applied to qubits only to implement the $R_x(\pi/2)$ single-qubit gate.

III. NOISE MODEL

Though there are a number of noteworthy sources of single-qubit decoherence, including leakage [15] and non-Markovian noise [28], we limit our attention to amplitude damping and phase damping, respectively characterized by IBM's publicly reported T_1 and T_2 coherence times.[2] Based on the physical implementation of IBM's native gates discussed in Section II, we model the noisy application of an $R_x(\pm\pi/2)$ gate as an instantaneous rotation, followed by decay and dephasing over time t_* equal to the gate duration. This is mathematically realized via the initial application of an $R_x(\pm\pi/2)$ unitary, followed by the appropriate Kraus operators. Accordingly, we model the noisy application of a single-qubit gate parameterized by Euler angles (β, γ, δ) by applying these Kraus operators after each instance of $R_x(\pm\pi/2)$ in Eq. (2); a pictorial representation can be found in Fig. 1. In this model, the noisy application of a single-qubit gate with Euler angles (β, γ, δ) will transform an initially pure state with Bloch sphere coordinates (θ, ϕ) into a mixed state with the following density matrix:

$$\rho_{(\beta, \gamma, \delta, \theta, \phi)} = \begin{bmatrix} a & b \\ b^* & 1-a \end{bmatrix} \tag{3}$$

$$a = \frac{1}{2}\Bigg[\Big(-\sin\gamma\cos(\phi+\delta)\sin\theta + \cos\gamma\cos\theta \Big) \\ \times (1-\lambda_A)^{3/2}\sqrt{1-\lambda_P} + 1 + \lambda_A \Bigg] \tag{4}$$

$$b = \frac{e^{-i\beta}}{2}\Bigg[\Big(\cos(\phi+\delta)\cos\gamma\sin\theta + \sin\gamma\cos\theta \Big) \\ \times (1-\lambda_A)(1-\lambda_P) \\ - i\Big(\sin(\phi+\delta)\sin\theta(1-\lambda_A) + \lambda_A \Big) \\ \times \sqrt{1-\lambda_A}\sqrt{1-\lambda_P} \Bigg] \tag{5}$$

This is explicitly derived in Appendix A. The variable λ_A is equal to the probability of a spontaneous emission during the application of an $R_x(\pm\pi/2)$ gate, and λ_P is equal to the probability of a spontaneous phase flip. Both

---

[1] Throughout this work, we use the terms single-qubit gate, rotation, and operation interchangeably.

[2] All single-qubit noise specifications for `ibmq_rome` [23] and `ibmq_bogota` [24] were provided by IBM through Qiskit [29] and are tabulated in Appendix E.
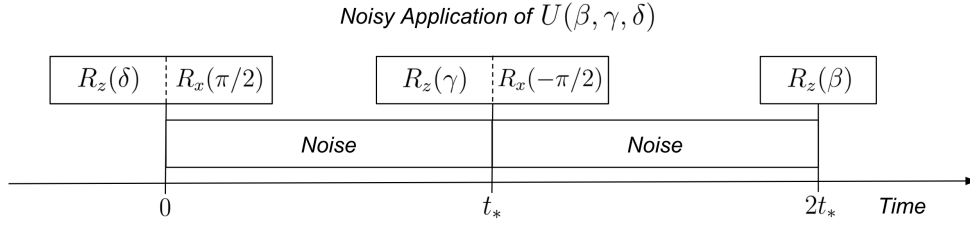
Figure 1. Noisy Gate Application: decomposition of single-qubit gate $U(\beta, \gamma, \delta)$ into native gates defined by Eq. (2); each R_z gate applied via noiseless frame change; each $R_x(\pm\pi/2)$ gate applied via microwave pulse and modeled as instantaneous rotation, followed by decoherence over time t_* equal to $R_x(\pm\pi/2)$ gate duration.

parameters are defined as functions of the system's T_1 and T_2 times, respectively, along with the aforementioned $R_x(\pm\pi/2)$ gate duration t_*:

$$\lambda_A = 1 - e^{-t_*/T_1} \tag{6}$$

$$\lambda_P = 1 - e^{-t_*/T_2} \tag{7}$$

IV. OPTIMIZATION

Using the noise model in Eqs. (3–5), we now outline a protocol by which the fidelity of an arbitrary single-qubit gate can be improved. Suppose we wish to implement the target operation $U(\beta_t, \gamma_t, \delta_t)$ acting on the initially pure state with Bloch sphere coordinates (θ, ϕ), represented below by $|\psi(\theta, \phi)\rangle$. Our protocol amounts to maximizing the following fidelity over the Euler angles (β, γ, δ):

$$F(\beta_t, \gamma_t, \delta_t, \beta, \gamma, \delta, \theta, \phi) =$$
$$\langle \psi(\theta, \phi)| U(\beta_t, \gamma_t, \delta_t)^\dagger \rho_{(\beta, \gamma, \delta, \theta, \phi)} U(\beta_t, \gamma_t, \delta_t) |\psi(\theta, \phi)\rangle \tag{8}$$

We find the optimal Euler angles $(\beta', \gamma', \delta')$ via gradient descent over the parameters (β, γ, δ). In the presence of noise, the native gate decomposition of $U(\beta', \gamma', \delta')$ will map the initial state $|\psi(\theta, \phi)\rangle$ to the target state $U(\beta_t, \gamma_t, \delta_t) |\psi(\theta, \phi)\rangle$ with higher fidelity than the default decomposition of $U(\beta_t, \gamma_t, \delta_t)$. We note that Eq. (8) has an explicit closed form.

To provide some intuition as to how an optimized operation achieves an improvement in fidelity, we begin by noting that the effect of amplitude damping is most pronounced on the south pole of the Bloch sphere (excited state), and the effect of phase damping is most pronounced on the equator of the Bloch sphere. Thus, to best map the initial state to the target state, the optimizer finds a trajectory through the Bloch sphere that most aptly avoids these noisy regions. For the sake of visualization, we have included an example of an optimized (blue) and an unoptimized (red) trajectory through the Bloch sphere in Fig. 2, wherein the optimized trajectory tends towards the coherent north pole more than its unoptimized counterpart. Figure generated using QuTiP [30, 31].
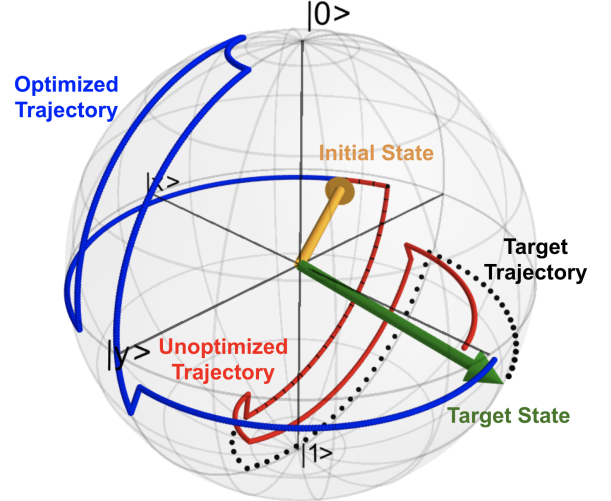

Figure 2. Optimized vs. Unoptimized Trajectories: optimized trajectory (blue) and unoptimized trajectory (red) mapped through the Bloch sphere in the presence of noise simulated from exaggerated `ibmq_rome` qubit 3 coherence times ($T_{1,2}/100$); initial state in orange; target trajectory dotted in black; target state in green. To maximize fidelity, the optimized trajectory avoids regions of the Bloch sphere (south pole and equator) that are more susceptible to noise.

V. ERROR RATE REDUCTION ON `IBMQ_ROME`

We now experimentally validate the protocol outlined in Section IV on `ibmq_rome` qubit 3 by empirically determining the reduction in the single-qubit error rate achieved by the optimizer. Since the qubit has $T_1 = 46.4\mu s$, $T_2 = 105\mu s$, pulse duration $t_* = 35.6ns$, and therefore damping probabilities $\lambda_A = 7.7 \times 10^{-4}$ and $\lambda_P = 3.4 \times 10^{-4}$, see Eqs. (6–7), the fidelity improvement offered by the optimizer is small. We therefore detect the improvement in fidelity by accumulating it over a long sequence of gates in the RB experiment below.

We begin by generating a circuit composed of a sequence of randomized single-qubit gates $C = (G_1, ..., G_N)$ acting on the initial state $|\psi_0\rangle = |0\rangle$. To randomize each gate $G_i \in C$, we sample its axis of ro-
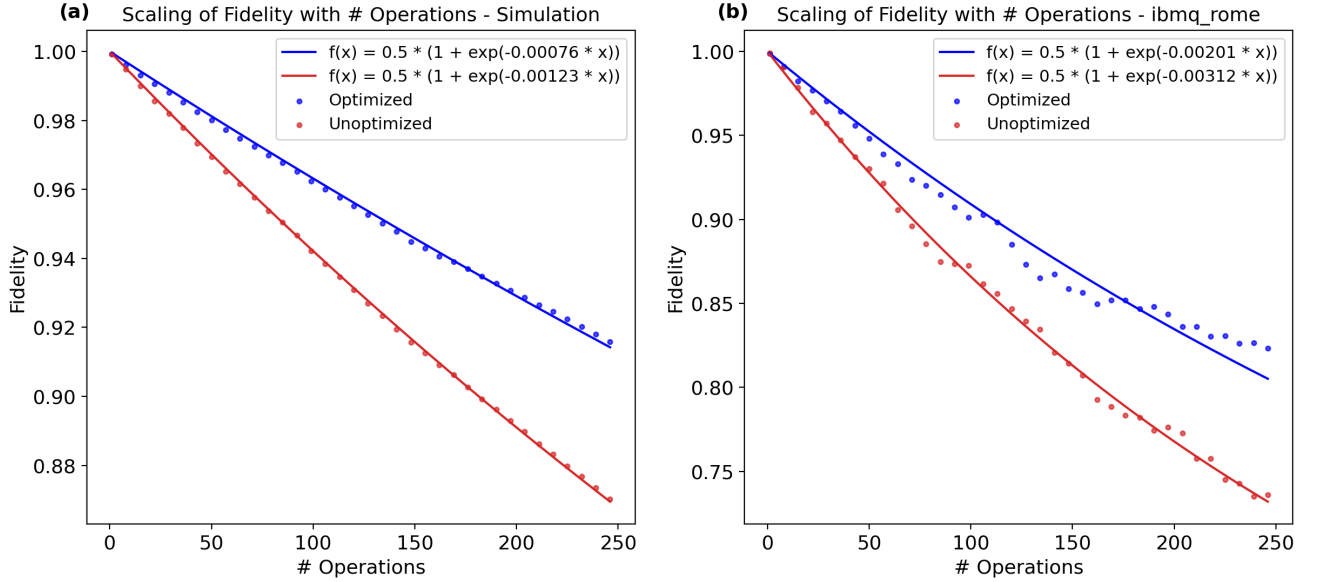
Figure 3. Scaling of Fidelity with # of Operations: 8192 shots per measurement taken at circuit depths of $d \in \{1, 8, 15, ..., 246\}$; resulting fidelities averaged over 10 randomized gate sequences. "# Operations" (horizontal axis) represents the depth at which the fidelity was measured; "Fidelity" (vertical axis) represents the overlap between the state output by the noisy application of each circuit (unoptimized and optimized) and the target state output by the noiseless application of the unoptimized circuit.

tation uniformly from the surface of the Bloch sphere and its angle uniformly from the interval $[0, 2\pi)$. We then optimize each gate G_i acting on the initial state $|\psi_{i-1}\rangle = G_{i-1}...G_1 |0\rangle$. The result is a new circuit C_{opt} composed of the optimized versions of the gates in the circuit C. For each circuit C and C_{opt}, we denote the subsequence composed of the first d gates by C^d and C^d_{opt}, respectively. We measure the unoptimized fidelity after d gates by applying C^d, then applying the 2-pulse native gate decomposition of $(C^d)^{-1}$, and then measuring the probability of collapse to $|0\rangle$. Similarly, we measure the optimized fidelity by applying C^d_{opt}, followed by $(C^d)^{-1}$, and then measuring the probability of collapse to $|0\rangle$. In the presence of noise, the subsequence that maps the $|0\rangle$ state closer to the target state $|\psi_d\rangle = C^d |0\rangle$ will return the higher probability of measuring $|0\rangle$ after $(C^d)^{-1}$ is applied. We generate 10 circuits, each consisting of $N = 246$ randomized rotations. For each of the 10 circuits, we measure the unoptimized and optimized fidelities at depths of $d \in \{1, 8, 15, ..., 246\}$. The empirically obtained fidelities at each depth d are then averaged over the 10 circuits.[3]

The results from simulating the execution of the circuits using our noise model and from executing the circuits on `ibmq_rome` qubit 3 are displayed in Fig. 3(a) and Fig. 3(b), respectively. In both plots, the blue points represent the fidelities of the optimized circuits, and the red

points represent the fidelities of the unoptimized circuits. The accumulation of noise in both circuits is reflected in the decrease in fidelity with circuit depth. We fit the data with the ansatz $f(x) = \frac{1}{2}(1 + \exp\{-ax\})$ because it satisfies the limiting cases $f(0) = 1$ and $\lim_{x \to \infty} f(x) = \frac{1}{2}$. Thus, the error rate of one randomized single-qubit gate is given by:

$$\text{error rate} = 1 - \text{fidelity} = 1 - f(1) \approx \frac{a}{2} \qquad (9)$$

In the simulation and on the hardware, the optimized circuit outperforms the unoptimized circuit, thereby experimentally validating the optimization protocol we outline in this work. Both the optimized and unoptimized circuits on the hardware have lower fidelities than the simulation; we attribute this to noise unaccounted for by our noise model. Finally, from direct calculation of the optimized and unoptimized error rates defined by Eq. (9), we conclude that on `ibmq_rome` qubit 3, our optimization protocol reduces the error rate of a single-qubit gate acting on a known initial state by 38%, from 1.6×10^{-3} to 1.0×10^{-3}. The unoptimized error rate that we report here does not agree with IBM's reported error rate of 3.4×10^{-4}. We attribute this discrepancy to differences in methodology when calculating error rates, as well as to the inaccuracy of our ansatz. That being said, we maintain our reported error rate reduction as an estimate for the degree to which the noise present during the execution of a single-qubit gate can be mitigated by leveraging knowledge of the initial state of the input qubit and a description of the noise present during gate execution. An experiment of identical structure was carried

---

[3] Readout errors were mitigated for all measurements made on `ibmq_rome` and `ibmq_bogota` by inverting a calibration matrix [32] composed of IBM's publicly reported readout error probabilities.
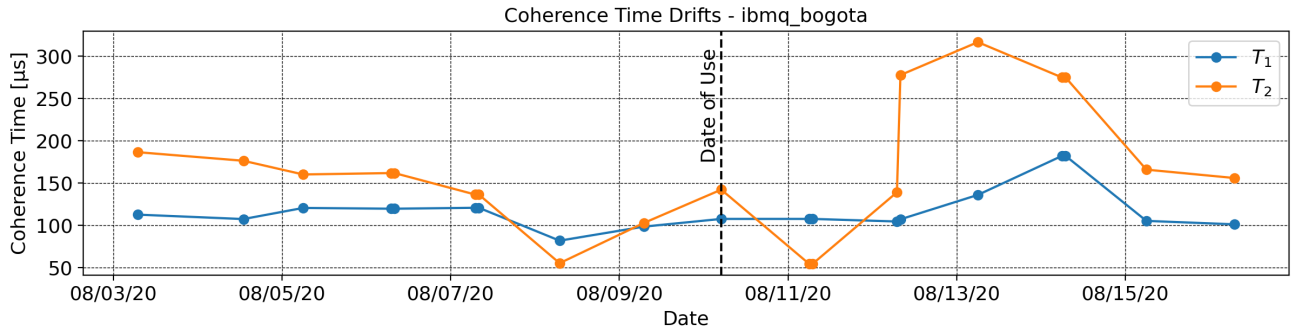
Figure 4. Coherence Time Drifts on `ibmq_bogota` qubit 2: IBM's publicly available T_1 and T_2 times obtained through Qiskit [29] up to one week before and after its date of use (08/10/20). "Date" (horizontal axis) represents the date of measurement "Coherence Time" (vertical axis) represents the coherence times measured (T_1 and T_2) on a given date.

out on Rigetti's Aspen-8 [33] device and is detailed in Appendix B.

VI. SENSITIVITY TO COHERENCE TIME DRIFTS ON IBMQ_BOGOTA

The optimization protocol outlined in this work reduces the error rate of a single-qubit gate by employing the T_1 and T_2 times characterizing the qubit's decoherence. These noise parameters are obtained empirically and are therefore subject to error as a result of coherence time drifts between measurements (see Fig. 4). One would hope that the protocol can improve gate fidelity even when the noise parameters being used are inaccurate. We now outline another RB experiment and demonstrate that the optimizer is resilient to coherence time drifts.

Since we cannot control the system's coherence times, we simulate the effect of a drift by intentionally providing the optimizer with inaccurate T_1 and T_2 times. Though these times drift independently, we simplify our experiment by simulating a simultaneous drift from their assumed values by a coherence time drift factor of k:

$$(\text{system } T_{1,2}) = k \times (\text{assumed } T_{1,2}) \qquad (10)$$

For each scaled pair of times assumed by the optimizer, we perform the same RB experiment outlined in Section V, now optimizing each gate in a 300-gate circuit and measuring the fidelity at depths of 100, 200, and 300 gates. The fidelities are once again averaged over 10 randomized gate sequences.

The results from simulating the execution of the circuits using our noise model and from executing the circuits on `ibmq_bogota` qubit 2 are displayed in Fig. 5(a) and Fig. 5(b), respectively. Each color corresponds to a particular circuit depth, as indicated by the legend. For each circuit depth, the corresponding dashed line represents the fidelity obtained without any optimization. The accumulation of noise in all circuits is reflected in the decrease in fidelity with circuit depth. As with the

experiment outlined in Section V, the fidelities gathered from the hardware are lower than those predicted by the simulation. We once again attribute this to noise unaccounted for by our noise model.

As k approaches 0, the optimizer assumes there is no noise in the system. For any target rotation, in the absence of noise, the optimal rotation is the target rotation itself. Thus, as k approaches 0, we expect the fidelity offered by the optimizer to approach the unoptimized fidelity. This holds true in both the simulation data and the hardware data. On the other hand, as k approaches ∞, the optimizer assumes an unrealistically large amount of noise in the system. The gradient descent discussed in Section IV is therefore performed over an assumed landscape unrepresentative of the system. The optimal rotation found by the optimizer will thus become uncorrelated with the target rotation, and the resulting fidelity will drop to 0.5, on average. This is reflected in both the simulation data and the hardware data; however, since this regime is impractical, we have omitted much of this fidelity drop-off for the sake of visualization. In between the extremes, we expect to see a fidelity greater than the unoptimized fidelity. Once again, this is reflected in both the simulation data and the hardware data. Most importantly, when the initial state of the input qubit is known, the optimizer will only decrease gate fidelity if the coherence times have drifted above 100 times their assumed values. Since such drastic drifts are unrealistic (see Fig. 4), we can rest assured that the optimizer will never decrease gate fidelity and is therefore resilient to coherence time drifts.

VII. OUTLOOK

The optimization protocol outlined in this work can be adapted for optimization over an arbitrary native gate set. First, we parameterize all decompositions of single-qubit gates into native gates. Next, we model the effect of noise during the execution of an arbitrary parameterized native gate sequence as it acts on a specified initial state
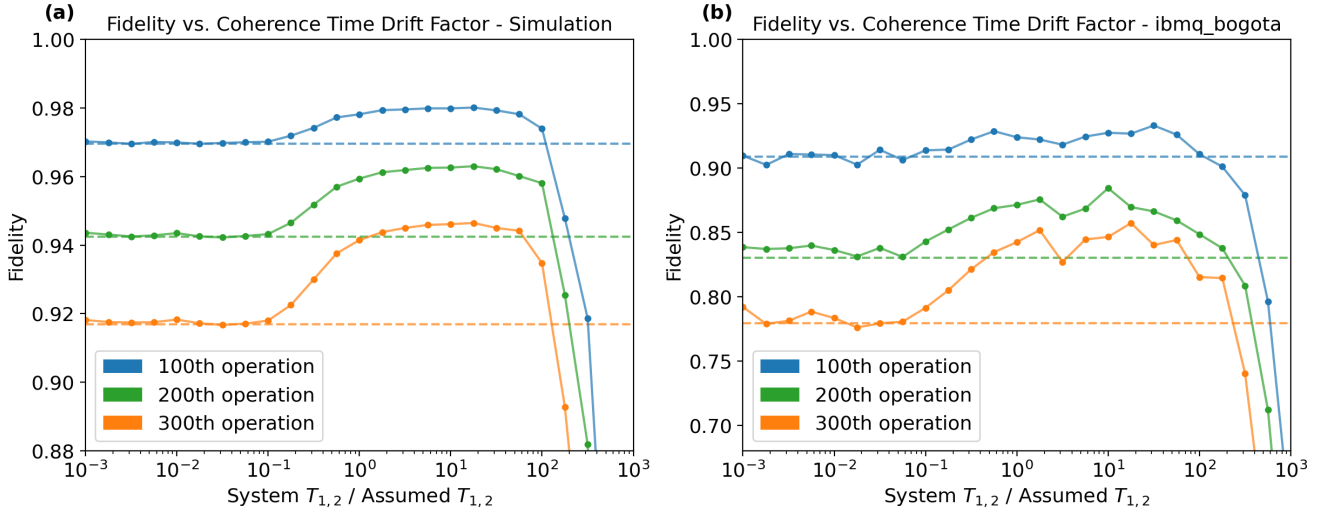
Figure 5. Fidelity vs. Coherence Time Drift Factor (System $T_{1,2}$ / Assumed $T_{1,2}$): 16384 shots per measurement taken at circuit depths of $d \in \{100, 200, 300\}$; resulting fidelities averaged over 10 randomized gate sequences; horizontal dashed lines represent unoptimized fidelities. "System $T_{1,2}$ / Optimizer $T_{1,2}$" (horizontal axis) represents the factor by which the system's coherence times differ from their assumed times during optimization; "Fidelity" (vertical axis) represents the overlap between the state output by the noisy application of the optimized circuit and the target state output by the noiseless application of the unoptimized circuit.

through the use of Kraus operators. Using this model, we compute the fidelity between the state output by a noiseless target operation acting on a known initial state and the state output by the noisy application of a variable operation acting on the same initial state. Finally, we maximize the fidelity over the parameters defining the variable operation by means of gradient descent to find the optimal operation to stand in place of the target operation in the presence of noise. We conclude our discussion of this protocol with three remarks. First, though the noise model used in this work was sufficient for proof of concept, the approximation that native gates are applied instantaneously and followed by decoherence over time equal to the gate duration can be avoided by deriving a noise model from master equations involving the system's Hamiltonian during gate execution (e.g., the Linbladian for Markovian environments). Second, as discussed in Appendix D, if the exact initial state of the input qubit is unknown, we can modify our optimization protocol to instead maximize the expected fidelity, averaged over the distribution of possible initial states. Third, the protocol can be adapted to optimize n-qubit gates by parameterizing all possible decompositions into an expanded native gate set (including entangling gates) and then proceeding as usual with the noise model and expected fidelity maximization for a specified distribution of n-qubit initial states. Since this work focused specifically on the optimization of single-qubit gates, gradient descent was sufficient for fidelity maximization; however, since the degrees of freedom required to parameterize an n-qubit gate are exponential in n, efficient alternatives to gradient descent are likely necessary to maximize the fidelity of larger n-qubit operations with more practical run-times.

The optimization of a single-qubit gate outlined in this work requires some knowledge of the input qubit's initial state, as detailed in Appendix D; despite this limitation, we now outline two potential applications of the optimization protocol. First, the protocol can be used to optimize the preparation of certain quantum states. For instance, since a product state is prepared via the parallel application of single-qubit gates, its fidelity can be increased by optimizing each single-qubit gate acting on the initial state $|0\rangle$. A detailed description of optimized single-qubit state preparation can be found in Appendix C. The protocol is therefore well-suited for use in Variational Quantum Eigensolvers (VQE)—currently one of the most promising practical applications of NISQ devices—since its performance relies heavily on high-fidelity state preparation often implemented through the initial preparation of a product state, followed by entangling operations [34]. Second, in the near-term, while the execution of quantum circuits can still be simulated by classical computers, we can track the state of each qubit and use our protocol to optimize an arbitrary gate embedded within a circuit. Though the input qubit to said gate will generally be entangled with other qubits in the circuit, its reduced density matrix can be recovered by tracing over the degrees of freedom introduced by the qubits with which it is entangled. Though this entanglement will cause the input qubit's initial state to be mixed, the optimization protocol can easily be adapted to accommodate mixed initial states, as alluded to in Appendix A. We emphasize that in the near-term, the protocol can be used to optimize all single-qubit gates on NISQ devices, beyond those involved in state preparation.

VIII.   CONCLUSION

The optimization protocol outlined in this work reduces the error rate of a single-qubit gate by leveraging knowledge of the initial state of the input qubit, along with a description of the noise in the system (T_1 and T_2 times). On `ibmq_rome` and `ibmq_bogota`, we proved the protocol can reduce the single-qubit error rate by 38%, from 1.6×10^{-3} to 1.0×10^{-3}, provided the initial state of the input qubit is known. On `ibmq_bogota`, we that the protocol will never decrease gate fidelity, provided the qubit's T_1 and T_2 times have not drifted above 100 times their assumed values. The protocol can improve the expected fidelity of a single-qubit gate provided *some* knowledge of the initial state of the input qubit—the more localized the initial state distribution, the more we can improve the expected fidelity. The protocol can be applied as a means to improve the fidelity of state preparation, as well as a means to improve the fidelity of quantum circuits for which some knowledge of intermediate states of qubits can be inferred; the former is well-suited for use in VQE, while the latter is likely only applicable in the near-term. This work presents a pathway to using information about noise levels and quantum state distributions to significantly reduce error rates associated with quantum gates via optimized decomposition into native gates.

[1] R. P. Feynman, Int. J. Theor. Phys **21** (1982).

[2] P. W. Shor, SIAM Journal on Computing **26**, 1484–1509 (1997).

[3] D. Loss and D. P. DiVincenzo, Phys. Rev. A **57**, 120 (1998).

[4] J. I. Cirac and P. Zoller, Phys. Rev. Lett. **74**, 4091 (1995).

[5] Y. Nakamura, Y. A. Pashkin, and J. S. Tsai, Nature **398**, 786 (1999).

[6] B. E. Kane, Nature **393**, 133 (1998).

[7] M. H. Devoret and R. J. Schoelkopf, Science **339**, 1169 (2013).

[8] G. Wendin, Reports on Progress in Physics **80**, 106001 (2017).

[9] P. Krantz, M. Kjaergaard, F. Yan, T. P. Orlando, S. Gustavsson, and W. D. Oliver, Applied Physics Reviews **6**, 021318 (2019).

[10] J. Preskill, Quantum **2**, 79 (2018).

[11] P. Jurcevic, A. Javadi-Abhari, L. S. Bishop, I. Lauer, D. F. Bogorin, M. Brink, L. Capelluto, O. Günlük, T. Itoko, N. Kanazawa, A. Kandala, G. A. Keefe, K. Krsulich, W. Landers, E. P. Lewandowski, D. T. McClure, G. Nannicini, A. Narasgond, H. M. Nayfeh, E. Pritchett, M. B. Rothwell, S. Srinivasan, N. Sundaresan, C. Wang, K. X. Wei, C. J. Wood, J.-B. Yau, E. J. Zhang, O. E. Dial, J. M. Chow, and J. M. Gambetta, Quantum Science and Technology **6**, 025020 (2021).

[12] S. Khatri, R. LaRose, A. Poremba, L. Cincio, A. T. Sornborger, and P. J. Coles, Quantum **3**, 140 (2019).

[13] P. Gokhale, A. Javadi-Abhari, N. Earnest, Y. Shi, and F. T. Chong, in *2020 53rd Annual IEEE/ACM International Symposium on Microarchitecture (MICRO)* (2020) pp. 186–200.

[14] A. R. R. Carvalho, H. Ball, M. J. Biercuk, M. R. Hush, and F. Thomsen, "Error-robust quantum logic optimization using a cloud quantum computer interface," (2020), arXiv:2010.08057 [quant-ph].

[15] M. Werninghaus, D. J. Egger, F. Roy, S. Machnes, F. K. Wilhelm, and S. Filipp, npj Quantum Information **7**, 1 (2021).

[16] J. J. Wallman and J. Emerson, Physical Review A **94**, 052325 (2016).

[17] B. Pokharel, N. Anand, B. Fortman, and D. A. Lidar, Physical Review Letters **121** (2018), 10.1103/physrevlett.121.220502.

[18] P. Magnard, P. Kurpiers, B. Royer, T. Walter, J.-C. Besse, S. Gasparinetti, M. Pechal, J. Heinsoo, S. Storz, A. Blais, and A. Wallraff, Phys. Rev. Lett. **121**, 060502 (2018).

[19] D. Egger, M. Werninghaus, M. Ganzhorn, G. Salis, A. Fuhrer, P. Müller, and S. Filipp, Phys. Rev. Applied **10**, 044030 (2018).

[20] F. Mallet, F. R. Ong, A. Palacios-Laloy, F. Nguyen, P. Bertet, D. Vion, and D. Esteve, Nature Physics **5**, 791 (2009).

[21] S. S. Elder, C. S. Wang, P. Reinhold, C. T. Hann, K. S. Chou, B. J. Lester, S. Rosenblum, L. Frunzio, L. Jiang, and R. J. Schoelkopf, Phys. Rev. X **10**, 011001 (2020).

[22] E. Knill, D. Leibfried, R. Reichle, J. Britton, R. B. Blakestad, J. D. Jost, C. Langer, R. Ozeri, S. Seidelin, and D. J. Wineland, Phys. Rev. A **77**, 012307 (2008).

[23] ibmq_rome v1.1.0, IBM Quantum team. Retrieved from https://quantum-computing.ibm.com (2020).

[24] ibmq_bogota v1.0.0, IBM Quantum team. Retrieved from https://quantum-computing.ibm.com (2020).

[25] M. A. Nielsen and I. Chuang, *Quantum computation and quantum information* (Cambridge University Press, 2002).

[26] A. W. Cross, L. S. Bishop, J. A. Smolin, and J. M. Gambetta, arXiv preprint arXiv:1707.03429 (2017).

[27] D. C. McKay, C. J. Wood, S. Sheldon, J. M. Chow, and J. M. Gambetta, Physical Review A **96**, 022330 (2017).

[28] H.-P. Breuer, E.-M. Laine, J. Piilo, and B. Vacchini, Rev. Mod. Phys. **88**, 021002 (2016).

[29] G. Aleksandrowicz, T. Alexander, P. Barkoutsos, L. Bello, Y. Ben-Haim, D. Bucher, F. Cabrera-Hernández, J. Carballo-Franquis, A. Chen, C. Chen,

et al., (2019), 10.5281/zenodo.2562110.

[30] J. R. Johansson, P. D. Nation, and F. Nori, Computer Physics Communications **183**, 1760 (2012).

[31] J. R. Johansson, P. D. Nation, and F. Nori, Computer Physics Communications **184**, 1234 (2013).

[32] B. Nachman, M. Urbanek, W. A. de Jong, and C. W. Bauer, npj Quantum Information **6**, 1 (2020).

[33] Rigetti Computing Quantum Cloud Services, http://qcs.rigetti.com, accessed August, 2020.

[34] A. Kandala, A. Mezzacapo, K. Temme, M. Takita, M. Brink, J. M. Chow, and J. M. Gambetta, Nature **549**, 242 (2017).

[35] S. Ashhab, J. Johansson, and F. Nori, New Journal of Physics **8**, 103 (2006).

[36] Y. M. Galperin, D. V. Shantsev, J. Bergli, and B. L. Altshuler, Europhysics Letters (EPL) **71**, 21 (2005).

[37] J. Majer, J. M. Chow, J. M. Gambetta, J. Koch, B. R. Johnson, J. A. Schreier, L. Frunzio, D. I. Schuster, A. A. Houck, A. Wallraff, and et al., Nature **449**, 443–447 (2007).

[38] R. S. Smith, M. J. Curtis, and W. J. Zeng, arXiv preprint arXiv:1608.03355 (2016).

[39] P. J. Karalekas, N. A. Tezak, E. C. Peterson, C. A. Ryan, M. P. da Silva, and R. S. Smith, Quantum Science and Technology **5**, 024003 (2020).

Appendix A: Noise Model Derivation

As discussed in Section III, we model the noisy application of an $R_x(\pm\pi/2)$ gate as an instantaneous rotation, followed by decay and dephasing over time t_* equal to the gate duration. Employing IBM's publicly available T_1 and T_2 times, along with the aforementioned gate duration t_*, we define the following Kraus operators for the amplitude damping and phase damping noise channels, respectively:

$$A_0 = \begin{bmatrix} 1 & 0 \\ 0 & \sqrt{1-\lambda_A} \end{bmatrix} \quad A_1 = \begin{bmatrix} 0 & \sqrt{\lambda_A} \\ 0 & 0 \end{bmatrix} \qquad (A1)$$

$$P_0 = \begin{bmatrix} 1 & 0 \\ 0 & \sqrt{1-\lambda_P} \end{bmatrix} \quad P_1 = \begin{bmatrix} 0 & 0 \\ 0 & \sqrt{\lambda_P} \end{bmatrix} \qquad (A2)$$

The variables λ_A and λ_P are defined in Eqs. (6–7), and their physical significance is described in Section III. Since the amplitude damping and phase damping superoperators commute, we can unambiguously define a mapping N that encapsulates the net effect of the two noise channels by applying one after the other, thereby mapping the density matrix

$$\rho = \begin{bmatrix} \rho_{00} & \rho_{01} \\ \rho_{10} & \rho_{11} \end{bmatrix} \qquad (A3)$$

to the density matrix

$$N(\rho) = \begin{bmatrix} \rho_{00}(1-\lambda_A) + \lambda_A & \rho_{01}\sqrt{1-\lambda_A}\sqrt{1-\lambda_P} \\ \rho_{10}\sqrt{1-\lambda_A}\sqrt{1-\lambda_P} & \rho_{11}(1-\lambda_A) \end{bmatrix} \qquad (A4)$$

Using this mapping and the decomposition defined by Eq. (2), we proceed by explicitly calculating the density matrix of a qubit after the noisy application of a single-qubit gate with Euler angles (β, γ, δ). If needed, we could begin with an initially mixed state parameterized by a 3-dimensional Bloch vector with length no more than unity, but for the sake of simplicity, we assume the input qubit is in an initially pure state with Bloch sphere coordinates (θ, ϕ). The initial state vector is given by the following:

$$|\psi(\theta,\phi)\rangle = \cos(\theta/2)|0\rangle + e^{i\phi}\sin(\theta/2)|1\rangle \qquad (A5)$$

The qubit's density matrix after the first pulse is given by:

$$\rho_1 = N(R_x(\pi/2)R_z(\delta)|\psi(\theta,\phi)\rangle\langle\psi(\theta,\phi)|R_z(\delta)^\dagger R_x(\pi/2)^\dagger) \qquad (A6)$$

After the second pulse:

$$\rho_2 = N(R_x(-\pi/2)R_z(\gamma)\rho_1 R_z(\gamma)^\dagger R_x(-\pi/2)^\dagger) \qquad (A7)$$

After the final $R_z(\beta)$ rotation:

$$\rho_{(\beta,\gamma,\delta,\theta,\phi)} = R_z(\beta)\rho_2 R_z(\beta)^\dagger \qquad (A8)$$

Applying these transformations, we find that the noisy application of a single-qubit gate parameterized by Euler angles (β, γ, δ) transforms an initially pure state with Bloch sphere coordinates (θ, ϕ) into a mixed state with the density matrix defined in Eqs. (3–5)

Throughout this derivation, we have implicitly assumed that the calibrated pulse amplitudes used to implement the $R_x(\pm\pi/2)$ gates in the presence of noise were exactly equal to the pulse amplitudes that would implement the $R_x(\pm\pi/2)$ gates perfectly in the absence of noise. This assumption is consistent with IBM's calibration methodology. IBM calibrates their $R_x(\pm\pi/2)$ gates by performing a Rabi experiment to determine the pulse amplitudes that most accurately implement them in the presence of noise [35–37]. Concretely, the optimal pulse is that which most accurately maps the $|0\rangle$ state to the state $R_x(\pm\pi/2)|0\rangle$ in the presence of noise. Within the framework of our noise model, since the angle of a noiseless R_x rotation is proportional to the amplitude of the pulse that implements it, finding the optimal pulse amplitude amounts to finding the optimal angle α that maximizes the following fidelity:

$$F = \langle 0| R_x(\pm\pi/2)^\dagger N(R_x(\alpha)|0\rangle\langle 0| R_x(\alpha)^\dagger)R_x(\pm\pi/2)|0\rangle$$
$$= \frac{1}{2}(1 \pm \sqrt{1-\lambda_A}\sqrt{1-\lambda_P}\sin\alpha)$$

$$(A9)$$

Since this achieves a maximum at $\alpha = \pm\pi/2$, it follows that the calibrated pulse amplitudes used to implement the $R_x(\pm\pi/2)$ gates in the presence of noise are exactly equal to the pulse amplitudes that would implement the $R_x(\pm\pi/2)$ gates perfectly in the absence of noise.

Appendix B: Error Rate Reduction on Aspen-8

As Rigetti's QCs are built from superconducting transmon qubits, their native gate set is identical to IBM's, allowing for easy adaptation of our protocol. An experiment of structure identical to that described in Section V was run on Rigetti's Aspen-8 qubit 4 [33].[4] The results are displayed in Fig. 6. An analysis of this data would mirror the analysis in Section V, so to avoid redundancy, we only discuss the reduction in error rate here.

On Aspen-8 qubit 4, our optimization protocol reduces the error rate of a single-qubit gate acting on a known initial state by 59%, from 8.2×10^{-3} to 3.4×10^{-3}. The unoptimized error rate that we report here does not agree with Rigetti's reported error rate of 7.5×10^{-3}, but there is better agreement than was found in on ibmq_rome.

---

[4] Readout error was mitigated for all measurements made on Aspen-8 by inverting a calibration matrix [32] composed of Rigetti's publicly reported readout error probabilities. All single-qubit noise specifications for Aspen-8 were provided by Rigetti through PyQuil [33, 38, 39] and are tabulated in Appendix E.
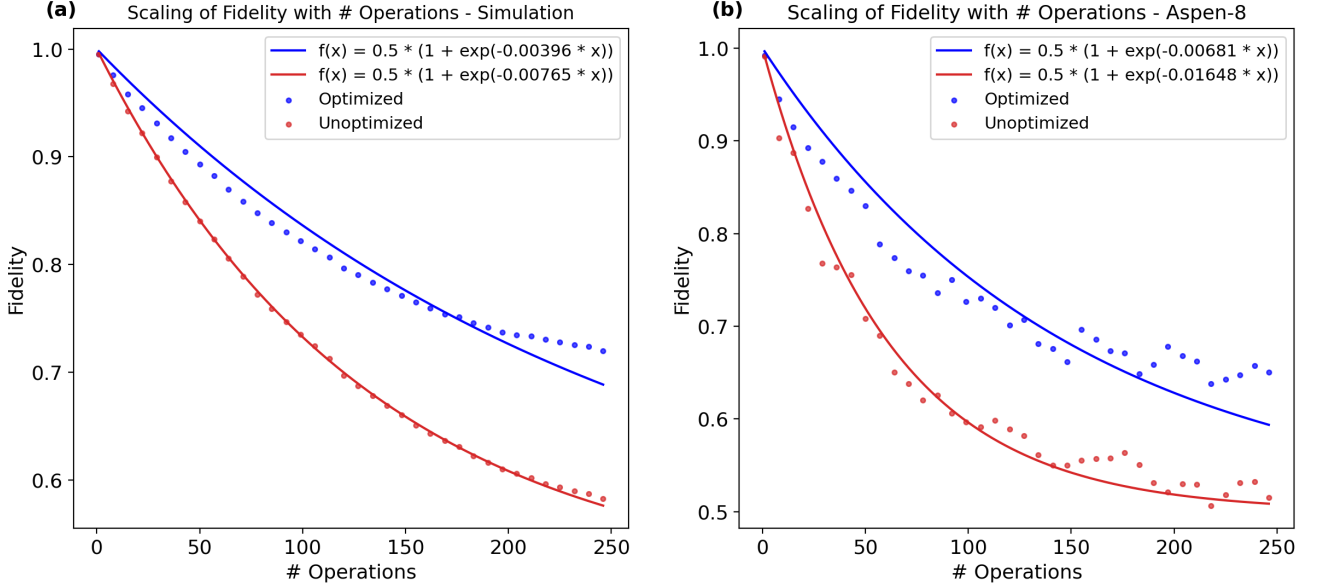
Figure 6. Scaling of Fidelity with # of Operations: 4096 shots per measurement taken at circuit depths of $d \in \{1, 8, 15, ..., 246\}$; resulting fidelities averaged over 10 randomized gate sequences. "# Operations" (horizontal axis) represents the depth at which the fidelity was measured; "Fidelity" (vertical axis) represents the overlap between the state output by the noisy application of each circuit (unoptimized and optimized) and the target state output by the noiseless application of the unoptimized circuit.

Appendix C: Single-Qubit State Preparation

As an illustrative example application of the optimization protocol outlined in Section IV, we now analyze its ability to improve the preparation fidelity of a single-qubit state. Suppose that we wish to implement the target operation $U(\phi_t, \theta_t, 0)$ mapping the initial state $|0\rangle$ to the target state with Bloch sphere coordinates (θ_t, ϕ_t):

$$|\psi(\theta_t, \phi_t)\rangle = U(\phi_t, \theta_t, 0) |0\rangle \qquad (C1)$$

Without loss of generality, we set $\delta = \theta = \phi = 0$ and reduce Eq. (8) to the following:

$$F(\theta_t, \phi_t, \beta, \gamma) = \langle\psi(\theta_t, \phi_t)| \rho_{(\beta,\gamma,0,0,0)} |\psi(\theta_t, \phi_t)\rangle \quad (C2)$$

We find the optimal Euler angles $(\beta', \gamma', 0)$ via gradient descent over the parameters β and γ. In the presence of noise, the native gate decomposition of $U(\beta', \gamma', 0')$ will map the initial state $|0\rangle$ to the target state $|\psi(\theta_t, \phi_t)\rangle$ with higher fidelity than the default decomposition of $U(\phi_t, \theta_t, 0)$.

We now proceed by analyzing the relationship between the improvement in preparation fidelity offered by the optimizer and the amount of noise in the system. Since λ_A and λ_P are typically on the same order of magnitude, we consider the improvement offered by optimization in the presence of noise parameterized by $\lambda = \lambda_A = \lambda_P$. For a fixed noise level λ, we randomly sample the target state $|\psi(\theta_t, \phi_t)\rangle$ uniformly from the surface of the Bloch sphere. We then find the aforementioned optimal angles β' and γ' and simulate the application of $U(\phi_t, \theta_t, 0)$ and $U(\beta', \gamma', 0)$ on the input $|0\rangle$. Finally, we calculate the percent improvement in fidelity to the target state $|\psi(\theta_t, \phi_t)\rangle$ and repeat this 100 times to calculate the average percent improvement in fidelity. The results from simulating the state preparation over a range of possible noise levels λ are displayed in Fig. 7.

Appendix D: Knowledge of the Initial State

The optimization protocol outlined in Section IV requires knowledge of the initial state to achieve an improvement in fidelity, as reflected in the fidelity function's explicit dependence on the initial state's Bloch sphere coordinates (see Eq. (8)). That being said, perfect knowledge of the initial state is not necessarily required for optimization. Provided a probability density function $p(\theta, \phi)$ for the distribution of the initial state over the Bloch sphere, we can optimize the target operation $U(\beta_t, \gamma_t, \delta_t)$ by maximizing the expected fidelity:

$$EF(\beta_t, \gamma_t, \delta_t, \beta, \gamma, \delta) =$$
$$\int_0^{2\pi} \int_0^{\pi} F(\beta_t, \gamma_t, \delta_t, \beta, \gamma, \delta, \theta, \phi) p(\theta, \phi) d\theta d\phi \qquad (D1)$$

The fidelity function $F(\beta_t, \gamma_t, \delta_t, \beta, \gamma, \delta, \theta, \phi)$ is defined in Eq. (8). We find the optimal Euler angles $(\beta', \gamma', \delta')$ via gradient descent over the parameters (β, γ, δ). In the presence of noise, the native gate decomposition of $U(\beta', \gamma', \delta')$ will on average map an initial state $|\psi(\theta, \phi)\rangle$ sampled from the distribution defined by $p(\theta, \phi)$ to the target state $U(\beta_t, \gamma_t, \delta_t) |\psi(\theta, \phi)\rangle$ with higher fidelity than the default decomposition of $U(\beta_t, \gamma_t, \delta_t)$.
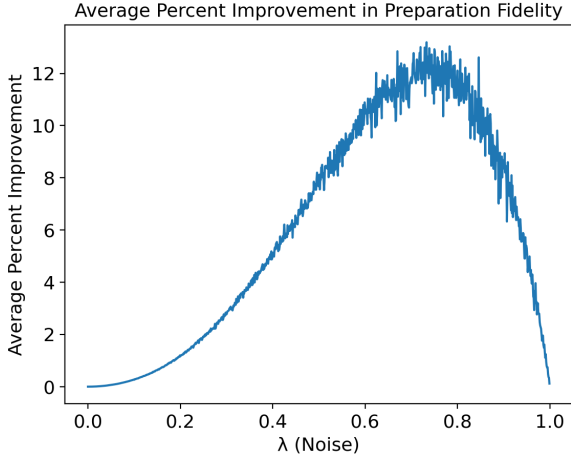
Figure 7. Average percent improvement in preparation fidelity: 100 randomly sampled target states per noise level λ, 1,000 total, evenly spaced noise levels (λ values). "λ" (horizontal axis) represents the amount of noise in the system; "Percent Improvement" (vertical axis) represents the percent improvement in preparation fidelity offered by the optimizer, averaged over 100 randomly sampled target states.

We proceed by analyzing the expected fidelity improvement offered by our protocol as a function of the initial state uncertainty. We have already shown a nontrivial improvement in expected fidelity provided perfect knowledge (i.e., minimal uncertainty) of the initial state $|0\rangle$ in Appendix C. The other extreme corresponds to no knowledge (i.e., maximal uncertainty) of the initial state and is represented by the distribution in which all states are equally likely:

$$p(\theta, \phi) = \frac{1}{4\pi} \sin\theta \tag{D2}$$

The expected fidelity in this case is given by

$$EF(\beta_{\mathrm{t}}, \gamma_{\mathrm{t}}, \delta_{\mathrm{t}}, \beta, \gamma, \delta) = \\ \frac{1}{4\pi} \int_0^{2\pi} \int_0^\pi F(\beta_{\mathrm{t}}, \gamma_{\mathrm{t}}, \delta_{\mathrm{t}}, \beta, \gamma, \delta, \theta, \phi) \sin\theta \, d\theta \, d\phi \tag{D3}$$

Further analysis shows

$$\left. \frac{\partial EF}{\partial \beta} \right|_{(\beta,\gamma,\delta)=(\beta_{\mathrm{t}},\gamma_{\mathrm{t}},\delta_{\mathrm{t}})} = 0 \tag{D4}$$

$$\left. \frac{\partial EF}{\partial \gamma} \right|_{(\beta,\gamma,\delta)=(\beta_{\mathrm{t}},\gamma_{\mathrm{t}},\delta_{\mathrm{t}})} = 0 \tag{D5}$$

$$\left. \frac{\partial EF}{\partial \delta} \right|_{(\beta,\gamma,\delta)=(\beta_{\mathrm{t}},\gamma_{\mathrm{t}},\delta_{\mathrm{t}})} = 0 \tag{D6}$$

Regardless of the target operation and the amount of noise, the expected fidelity achieves a local maximum at $(\beta, \gamma, \delta) = (\beta_{\mathrm{t}}, \gamma_{\mathrm{t}}, \delta_{\mathrm{t}})$. We deduce that our protocol
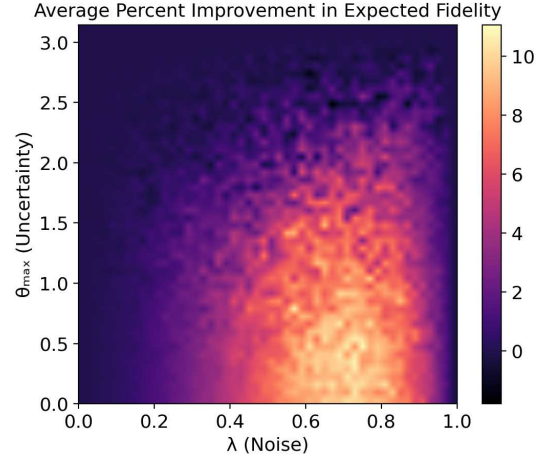

Figure 8. Average percent improvement in expected fidelity: 100 randomly sampled target operations + initial states per data point, 50x50 total data points. "λ" (horizontal axis) represents the amount of noise in the system; "$\theta_{\max}$" (vertical axis) represents the uncertainty in our knowledge of the initial state of the input qubit: $\theta_{\max} = 0$ corresponds to perfect knowledge of the initial state $|0\rangle$ and therefore recovery of Fig. 7; $\theta_{\max} = \pi$ corresponds to no knowledge of the initial state and therefore no improvement.

requires *some* knowledge of the initial state to improve expected fidelity.

To further analyze this dependence, we examine the effect of maximizing the expected fidelity for a new probability density function:

$$p(\theta, \phi) = \begin{cases} \frac{\sin\theta}{2\pi(1-\cos\theta_{\max})} & \text{if } \theta < \theta_{\max} \\ 0 & \text{if } \theta \geq \theta_{\max} \end{cases} \tag{D7}$$

The initial state is now uniformly distributed over the portion of the Bloch sphere with polar angle less than $\theta_{\max}$. Accordingly, as $\theta_{\max}$ approaches 0, we recover the case of state preparation, and for $\theta_{\max} = \pi$, we recover the case of maximal uncertainty. By varying $\theta_{\max}$ and examining its effect on the improvement in expected fidelity achieved by maximizing

$$EF(\beta_{\mathrm{t}}, \gamma_{\mathrm{t}}, \delta_{\mathrm{t}}, \beta, \gamma, \delta) = \\ \int_0^{2\pi} \int_0^{\theta_{\max}} \frac{F(\beta_{\mathrm{t}}, \gamma_{\mathrm{t}}, \delta_{\mathrm{t}}, \beta, \gamma, \delta, \theta, \phi) \sin\theta}{2\pi(1-\cos\theta_{\max})} d\theta \, d\phi \tag{D8}$$

we quantify the degree to which an arbitrary single-qubit gate can be optimized as a function of the initial state uncertainty.

To visualize this dependence, we begin by fixing the noise parameter $\lambda = \lambda_{\mathrm{A}} = \lambda_{\mathrm{P}}$ and the maximum polar angle $\theta_{\max}$. We proceed to randomly generate a target rotation $U(\beta_{\mathrm{t}}, \gamma_{\mathrm{t}}, \delta_{\mathrm{t}})$ by sampling the axis of rotation uniformly from the surface of the Bloch sphere and sampling the angle of rotation uniformly from the interval $[0, 2\pi)$. We then find the optimal Euler angles $(\beta', \gamma', \delta')$ via gradient descent over the parameters (β, γ, δ). Finally, we

sample the initial state $|\psi(\theta, \phi)\rangle$ uniformly from the portion of the Bloch sphere with polar angle less than $\theta_{\max}$, simulate the application of $U(\beta', \gamma', \delta')$ and $U(\beta_t, \gamma_t, \delta_t)$ in the presence of noise parameterized by λ, and calculate the percent improvement in fidelity to the target state $U(\beta_t, \gamma_t, \delta_t)|\psi(\theta, \phi)\rangle$. We note that this represents the percent improvement in expected fidelity due to the random sampling of the initial state. We repeat this for 100 randomized rotations and calculate the average percent improvement in expected fidelity. The results over a range of possible noise levels λ and polar angles $\theta_{\max}$ are displayed in Fig. 8. For $\theta_{\max} = 0$, we have perfect knowledge of the initial state $|0\rangle$ and accordingly recover

Fig. 7. For $\theta_{\max} = \pi$, we have no knowledge of the initial state and accordingly see no improvement in fidelity. Intuitively, the more we know about the initial state of the input qubit, the more we can fine-tune our optimization of the target operation to achieve a higher expected fidelity.

Appendix E: Noise Specifications

For all of the QCs used throughout this work, the single-qubit noise specifications on their respective dates of use are provided below.

Noise Specifications - ibmq_rome - 07/14/20						
Qubit	T_1 [μs]	T_2 [μs]	Pulse Duration [ns]	Prob. Prep. $|0\rangle$ Meas. $|1\rangle$	Prob. Prep. $|1\rangle$ Meas. $|0\rangle$	Gate Error [10^{-4}]
0	116	93.4	35.6	0.030	0.063	3.23
1	105	55.2	35.6	0.020	0.073	3.00
2	80.2	124	35.6	0.073	0.087	4.04
3	46.4	105	35.6	0.027	0.050	3.35
4	71.6	138	35.6	0.027	0.043	5.01
Mean	83.9	103	35.6	0.035	0.063	3.77
SD	27.7	31.7	0.00	0.022	0.017	0.798
Noise Specifications - ibmq_bogota - 08/10/20						
Qubit	T_1 [μs]	T_2 [μs]	Pulse Duration [ns]	Prob. Prep. $|0\rangle$ Meas. $|1\rangle$	Prob. Prep. $|1\rangle$ Meas. $|0\rangle$	Gate Error [10^{-4}]
0	126	158	35.6	0.024	0.108	5.10
1	117	168	35.6	0.004	0.039	2.36
2	107	142	35.6	0.009	0.026	2.19
3	199	240	35.6	0.005	0.034	3.96
4	142	249	35.6	0.019	0.135	2.02
Mean	138	192	35.6	0.012	0.068	2.63
SD	36.4	49.6	0.00	0.009	0.050	0.898
Noise Specifications - Aspen-8 - 08/30/20						
Qubit	T_1 [μs]	T_2 [μs]	Pulse Duration [ns]	Prob. Prep. $|0\rangle$ Meas. $|1\rangle$	Prob. Prep. $|1\rangle$ Meas. $|0\rangle$	Gate Error [10^{-4}]
0	16.9	18.7	60.0	0.014	0.034	50.0
1	36.7	40.4	60.0	0.049	0.063	4.00
2	18.5	12.1	60.0	0.017	0.033	112
3	34.2	19.5	60.0	0.022	0.046	13.0
4	15.3	17.6	60.0	0.017	0.034	75.0
5	41.4	5.37	60.0	0.047	0.075	5.00
6	45.0	45.1	60.0	0.015	0.042	31.0
7	17.2	22.8	60.0	0.016	0.038	11.0
11	23.8	12.7	60.0	0.058	0.058	10.0
12	21.6	8.18	60.0	0.034	0.134	27.0
13	27.0	18.3	60.0	0.040	0.056	26.0
14	17.9	11.3	60.0	0.018	0.037	40.0
15	35.9	3.76	60.0	0.035	0.066	16.0
16	21.8	28.6	60.0	0.009	0.037	24.0
17	37.9	14.7	60.0	0.021	0.042	13.0
20	18.7	15.7	60.0	0.017	0.041	19.0
21	43.7	7.29	60.0	0.045	0.082	32.0
22	29.6	25.3	60.0	0.035	0.072	19.0
23	24.8	9.89	60.0	0.074	0.078	1034
24	12.9	2.18	60.0	0.042	0.116	18.0
25	42.9	20.4	60.0	0.035	0.060	10.0
26	10.6	2.22	60.0	0.015	0.047	79.0
27	43.1	18.7	60.0	0.036	0.074	8.00
30	21.1	26.3	60.0	0.040	0.178	70.0
31	42.0	37.2	60.0	0.035	0.092	5.00
32	43.1	56.8	60.0	0.022	0.076	10.0
33	29.0	27.0	60.0	0.027	0.080	9.00
34	17.9	21.0	60.0	0.010	0.034	15.0
35	30.5	35.3	60.0	0.052	0.091	2.00
36	33.8	23.4	60.0	0.041	0.091	45.0
37	35.3	22.8	60.0	0.041	0.053	10.0
Mean	28.7	20.3	60.0	0.032	0.066	59.4
SD	10.7	12.8	0.00	0.016	0.033	183